

17 **Abstract**

18 Seismic full waveform inversion (FWI) is a powerful tool for monitoring subsurface
19 changes during carbon capture and storage (CCS) operations, but its ill-posed nature
20 makes uncertainty quantification (UQ) essential for reliable interpretation.
21 Sampling-based Bayesian methods such as Markov chain Monte Carlo (MCMC)
22 provide rigorous UQ but are computationally demanding. In conventional FWI,
23 elastic properties are assigned to densely discretized space-filling cells, resulting in
24 a high-dimensional parameterization that makes large-scale elastic FWI
25 computationally infeasible. To address this challenge, we propose a rock-physics-
26 guided parameter-reduction strategy that compactly represents the CO₂ plume
27 geometry using cubic splines controlled by a limited number of nodes. This
28 parsimonious parameterization not only significantly reduces the number of model
29 parameters and the forward simulations required for effective UQ using sampling
30 methods but also has the potential to improve the practicality and efficiency of other
31 types of UQ methods. Numerical experiments on a cross-well synthetic scenario and
32 a field-scale synthetic case based on the Aquistore storage site in Saskatchewan,
33 Canada, demonstrate that the method efficiently reconstructs the plume shape and
34 its extent and that it converges to consistent posterior distributions across multiple
35 Markov chains.

36 **Introduction**

37 Geophysical surveys are essential for imaging and tracking subsurface changes. This
38 is typically achieved through an inversion that recovers the physical properties and
39 geometry of the subsurface. In seismic methods, full waveform inversion (FWI) is a
40 leading inversion technique for reconstructing detailed, high-resolution models of
41 the subsurface using complete waveform information (Fichtner et al. 2009; Virieux
42 and Operto 2009). FWI has also been extended to time-lapse imaging, where
43 changes in the subsurface are estimated via repeated seismic surveys (Plessix et al.
44 2010; Asnaashari et al. 2012; 2015; Kotsi and Malcolm 2017). FWI has also proven
45 highly effective for CO₂ monitoring (Queißer and Singh 2013; Zhang et al. 2013;
46 Egorov et al. 2017). However, similar to other inverse problems, FWI is inherently
47 ill-posed, which means many plausible models can explain the data equally well
48 within noise limits (Mosegaard and Sambridge 2002; Tarantola 2005). This
49 ambiguity emphasizes the need to explore not just a single “best-fit” model, as in
50 deterministic FWI, but rather the range of models consistent with observations.

51 To study and understand the range of plausible models of subsurface properties that
52 are consistent with the observed data, various uncertainty quantification (UQ)
53 techniques based on Bayes' theorem have been developed (Mosegaard and
54 Sambridge 2002; Sambridge and Mosegaard 2002). For example, Markov chain
55 Monte Carlo (MCMC) sampling methods enable estimation of the so-called *posterior*

56 probability distribution function (PDF) (Tarantola 2005; Sen and Stoffa 2013;
57 Fichtner and Simutè 2018; Kotsi et al. 2020; Li and Innanen 2024). However, McMC
58 becomes impractical as the dimensionality increases. This is because the number of
59 samples required to efficiently explore the search space and thus adequately
60 reconstruct the posterior distribution substantially increases with the dimensionality
61 of the problem as it takes more time for the Markov chain to reach equilibrium
62 (Gelman et al. 1997; Brooks et al. 2011). Consequently, at least hundreds of
63 thousands of proposed samples must be evaluated while typically only up to 25% of
64 them are accepted (Roberts and Rosenthal 2001).

65 Like most geophysical inversions, elastic FWI (eFWI) is typically performed on
66 meshes of space-filling cells such as hexahedra or tetrahedra, where the elastic
67 properties of each cell are unknown. As a result, eFWI is a high-dimensional inverse
68 problem. Despite advances in high-performance computing, since hundreds of
69 thousands of elastic wave equation solves are required to adequately sample the
70 posterior PDF, Bayesian eFWI is computationally infeasible (Mohammadi et al.
71 2025a).

72 To reduce the complexity and computational cost of inversion in geophysical
73 methods, a wide range of various parameterization schemes and inversion strategies
74 have been developed to represent subsurface structures with fewer degrees of
75 freedom (DoF) (Vatankhah et al. 2025). Early studies focused on recovering the

76 shape of anomalies directly using gravity data (René 1986). Later approaches
77 introduced iterative feature planting and growth in gravity inversion (Uieda and
78 Barbosa 2012). Further, level-set formulations for multi-physics problems have also
79 been proposed (Zheglova and Farquharson 2016; Zheglova et al. 2018). In recent
80 studies, direct shape reconstruction through explicit boundary parametrization has
81 also been proposed (Bijani et al. 2017; Galley et al. 2020). In the FWI community,
82 various studies use level-set methods for salt reconstruction (Lewis et al. 2012; 2012;
83 Kadu et al. 2016; Dorn and Wu 2021).

84 Since, for CO₂ sequestration, some of the sought-after parameters (e.g., physical
85 properties) are already known from rock-physics simulations and measurements, our
86 goals may be simply to place constraints on the shape or extent of a known body
87 (i.e., the CO₂ plume here) (Mito and Xue 2011; Macquet et al. 2019; Prasad et al.
88 2021; Mohammadi et al. 2025b; Entezar-Saadat et al. 2025). Thus, similar to
89 previous parameterization approaches, to address the computational cost of eFWI in
90 CO₂ monitoring, we develop a tractable, uncertainty-aware parameterization scheme
91 that is explicitly guided by rock physics principles relevant to CO₂ storage and
92 monitoring. Our approach drastically reduces the number of DoF while maintaining
93 physical interpretability, making UQ with MCMC feasible. While broadly
94 applicable, we demonstrate the method for CO₂ sequestration, where prior geological
95 and geophysical knowledge is often substantial. Using a synthetic model of the

96 Aquistore CO₂ storage site in Saskatchewan, Canada, which is a field that has stored
97 over 600,000 tonnes of CO₂ (Vahidinia et al. 2024), we show how prior information
98 can be efficiently incorporated into a UQ framework with MCMC. To do so, first we
99 frame the time-lapse eFWI problem in a Bayesian inference context using the
100 adaptive MCMC algorithm (Haario et al. 2001a). Then we discuss our
101 parameterization scheme, followed by simple and Aquistore-inspired examples.
102 Finally, we discuss the results and present our conclusions.

103 **4D Bayesian FWI**

104 In FWI, we aim to estimate the subsurface model parameters $\boldsymbol{\theta} \in \mathbb{R}^m$ from the
105 observations $\mathbf{d}^{\text{obs}} \in \mathbb{R}^n$, where m and n are the dimensions of the model space and
106 observed seismic data, respectively. Using Bayes' theorem, which describes the
107 relationship between a hypothesis and given evidence, we formulate FWI as a
108 Bayesian inference problem (Tarantola 2005):

$$p_{\text{post}}(\boldsymbol{\theta}|\mathbf{d}^{\text{obs}}) = \frac{p_{\text{like}}(\mathbf{d}^{\text{obs}}|\boldsymbol{\theta})p_{\text{prior}}(\boldsymbol{\theta})}{p(\mathbf{d}^{\text{obs}})}, \quad (1)$$

109 where p is a probability density function (PDF), $p_{\text{post}}(\boldsymbol{\theta}|\mathbf{d}^{\text{obs}})$ and $p_{\text{like}}(\mathbf{d}^{\text{obs}}|\boldsymbol{\theta})$
110 are the posterior and likelihood PDFs, respectively. Our aim is to estimate the
111 posterior PDF, which describes the probability of the subsurface model parameters
112 $\boldsymbol{\theta}$ representing the true model, given the observations \mathbf{d}^{obs} . To make this estimate,
113 we use the likelihood PDF, which describes the probability of observing the seismic

114 data \mathbf{d}^{obs} given the subsurface model parameters $\boldsymbol{\theta}$, and $p_{\text{prior}}(\boldsymbol{\theta})$ which describes
 115 the prior PDF. Here $p(\mathbf{d}^{\text{obs}})$ is the evidence, which is considered to be a
 116 normalization constant, and the prior PDF is a uniform distribution (Tarantola 2005).
 117 Following (Kotsi and Malcolm 2017), we write Equation (1) in terms of model and
 118 data perturbations

$$p_{\text{post}}(\boldsymbol{\delta\theta}|\boldsymbol{\delta\mathbf{d}}) = \frac{p_{\text{like}}(\boldsymbol{\delta\mathbf{d}}|\boldsymbol{\delta\theta})p_{\text{prior}}(\boldsymbol{\delta\theta})}{p(\boldsymbol{\delta\mathbf{d}})}. \quad (2)$$

119 The likelihood PDF we use in Equation (2) is

$$\mathcal{L}(\boldsymbol{\delta\theta}) \equiv p_{\text{like}}(\boldsymbol{\delta\mathbf{d}}|\boldsymbol{\delta\theta}) \propto \exp\left[-\frac{1}{2}(\mathbf{F}(\boldsymbol{\delta\theta}) - \boldsymbol{\delta\mathbf{d}})^T \boldsymbol{\Sigma}^{-1}(\mathbf{F}(\boldsymbol{\delta\theta}) - \boldsymbol{\delta\mathbf{d}})\right], \quad (3)$$

121 where \mathbf{F} is the forward operator that calculates the seismic data based on perturbed
 122 subsurface model parameters $\boldsymbol{\delta\theta}$, and $\boldsymbol{\Sigma}^{-1}$ is the inverse of the covariance matrix of
 123 the noise in the observations. Note that the likelihood calculation in Equation (3) is
 124 performed by evaluating the forward model over the full model domain. The
 125 parameter vector $\boldsymbol{\delta\theta}$ only specifies perturbations to the baseline model and does not
 126 restrict the forward simulation itself.

127 Assuming that the proposal distribution, which is the distribution we use for drawing
 128 samples from the prior, is symmetric (i.e., Gaussian) and the prior PDF is bounded,
 129 to efficiently explore the search space and have a higher effective sample size than

130 random walk Metropolis-Hastings (MH), we use adaptive MH (Haario et al. 2001).

131 The proposed candidate at each iteration is

$$\delta\theta_i \sim \mathcal{N}(\delta\theta_j, \sigma_t) \quad (4)$$

132 where we choose \mathcal{N} to be the Normal distribution with standard deviation σ_t , while

133 i and j indicate the proposed and current candidates, respectively. To either accept

134 or reject a candidate, we use the MH acceptance criteria

$$\alpha = p(\delta\theta_i|\delta\theta_j) = \min \left[1, \frac{p_{\text{like}}(\delta\mathbf{d}|\delta\theta_i)}{p_{\text{like}}(\delta\mathbf{d}|\delta\theta_j)} \right], \quad (5)$$

135 where p , α , i and j indicate the acceptance probability, acceptance ratio, proposed

136 and current subsurface model parameters (Metropolis et al. 1953; Hastings 1970;

137 Mosegaard and Tarantola 1995).

138 **CO₂ Plume Parametrization**

139 Using the rock-physics models describing the behavior of injected CO₂, such as the

140 Biot-Gassmann equation (Biot 1941; Gassmann 1951), which assumes that rocks are

141 isotropic and homogeneous, we can calculate the expected changes in density, P-

142 and S-wave velocities in either brine- or hydrocarbon-filled reservoirs as a function

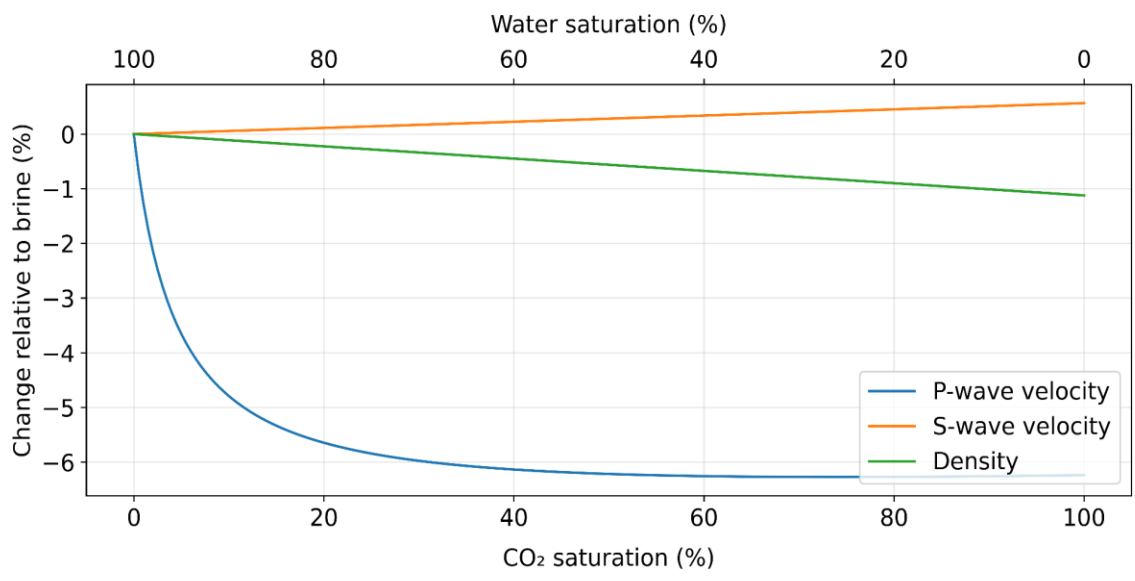
143 of fluid saturation (Mavko et al. 2020). As an example, we have done this for the

144 Aquistore storage site. Figure 1 shows these changes as a function of CO₂ saturation

145 for our synthetic simulations (with reservoir parameters given in Table 1); the

146 expected changes in physical properties are limited. Changes in density and S-wave

147 velocity are small enough that we can safely ignore them. Further, we assign a single
148 velocity value to the entire plume and treat it as a homogeneous body, as the change
149 in P-wave velocity after approximately 20% of CO₂ saturation is negligible. Due to
150 the physical behavior of structurally trapped CO₂, particularly its buoyancy, the
151 injected CO₂ tends to migrate upward and accumulate beneath the primary seal (i.e.,
152 the immediate caprock) after injection.



153
154 *Figure 1. Changes in seismic properties as a function of CO₂ saturation. For the physical properties we*
155 *used, please see Table 1.*

156 This predictable migration pattern, also seen by Yordkayhun et al. (2009) and
157 Harvey et al. (2022), enables us to parameterize the plume based on its physical
158 boundaries, using topologically consistent geometric models that are constrained by
159 the primary seal unit. These models are defined by a discrete set of what we call
160 *control-nodes*, which serve as structural anchors, as illustrated in Figure 2. The

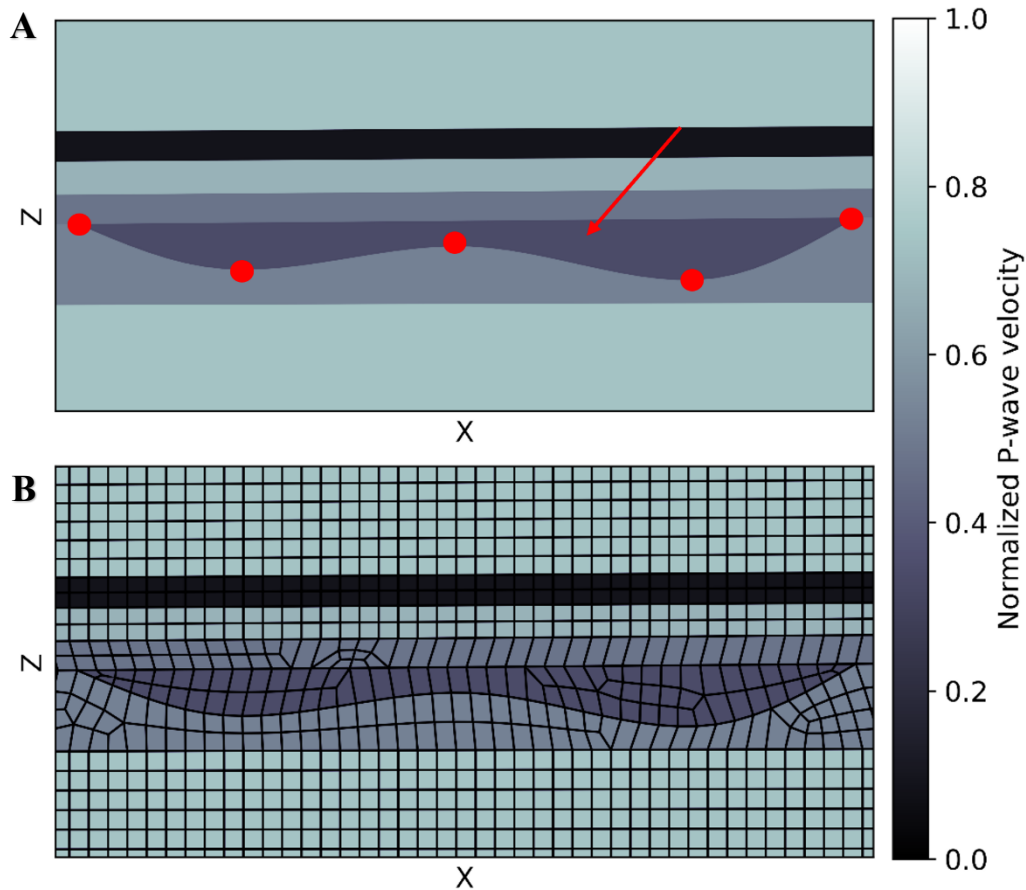
161 boundaries, or facets between control nodes, are then constructed using cubic
162 splines. This ensures smooth and continuous transitions between control nodes while
163 passing through every control node (Bartels et al. 1995; Schumaker 2015). Using
164 this scheme, we define the model parameter vector $\boldsymbol{\theta} \in \mathbb{R}^m$ in a general form as

$$\boldsymbol{\theta} = (x_1, z_1, x_2, z_2, \dots, x_m, z_m), \quad (6)$$

165 where (x_i, z_i) are the coordinates of the i^{th} control node. Although each node is, in
166 principle, allowed to move freely during UQ, in some of our examples, because we
167 are monitoring structurally trapped CO_2 in the subsurface, some nodes are
168 constrained and can only move on specific curves, the locations of which are
169 considered *a priori* information. A simpler alternative is introducing regular shapes
170 such as semi-ellipses to construct CO_2 plumes. We demonstrate this in our first
171 example.

172 Since in our parameterization scheme we introduce both regular and irregular
173 geometries during the stochastic inversion, we use the spectral finite element method
174 with unstructured quadrilateral meshes generated by Coreform Cubit 2024.3, to
175 accurately model elastic wave propagation and represent complex boundaries
176 (Komatitsch and Tromp 1999; Tromp et al. 2008; Peter et al. 2011). Figure 2a
177 illustrates an arbitrarily defined shape generated using our proposed method with a
178 small set of control nodes, while Figure 2b shows the same shape represented with

179 the space-filling cells used for forward modeling. The latter results in a substantially
180 larger number of DoF to approximate the same geometry.



181
182 *Figure 2. Parameterization comparison between (A) control-nodes (illustrated with red circles) and (B)*
183 *space-filling unstructured cells for an arbitrarily defined shape (illustrated with a red arrow).*

184 **Examples**

185 **Cross-well FWI**

186 For our first example, we generate a semi-elliptical CO₂ plume. Figure 3a shows the
187 baseline P-wave velocity model. For the monitoring model, as shown in Figure 3b,
188 we add an elliptical perturbation at the center of the domain representing the plume.

189 This perturbation is defined by the following two parameters: (1) the ellipse center
190 position and (2) the major radius. For simplicity, we keep the minor radius fixed.

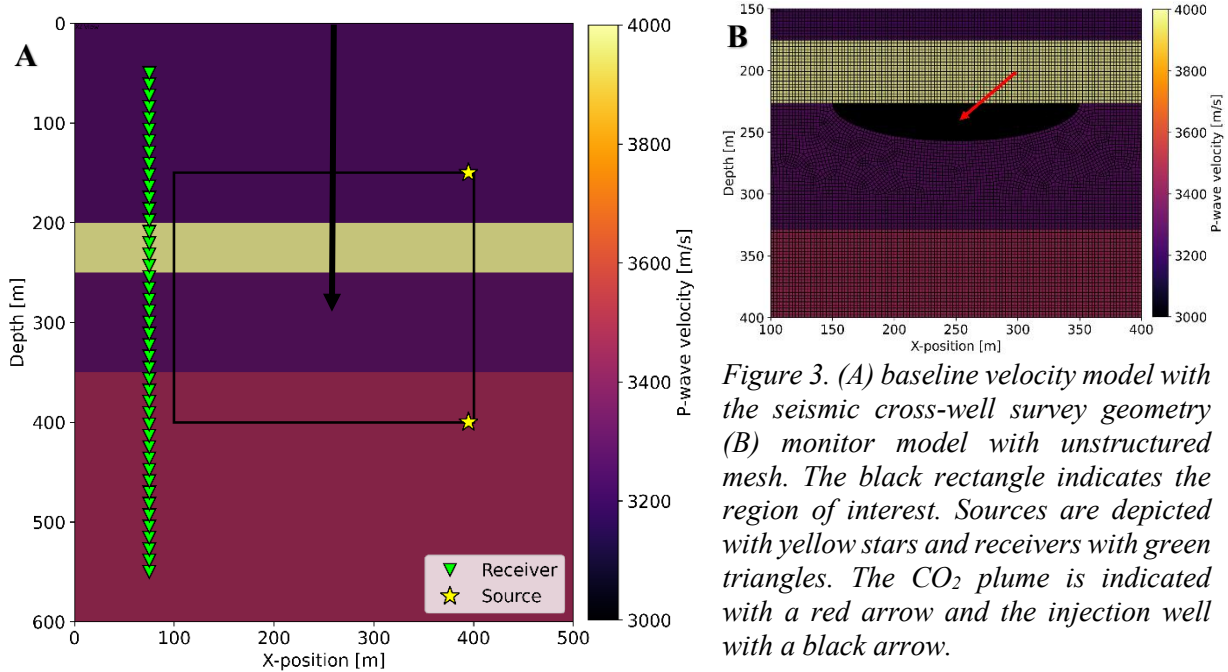
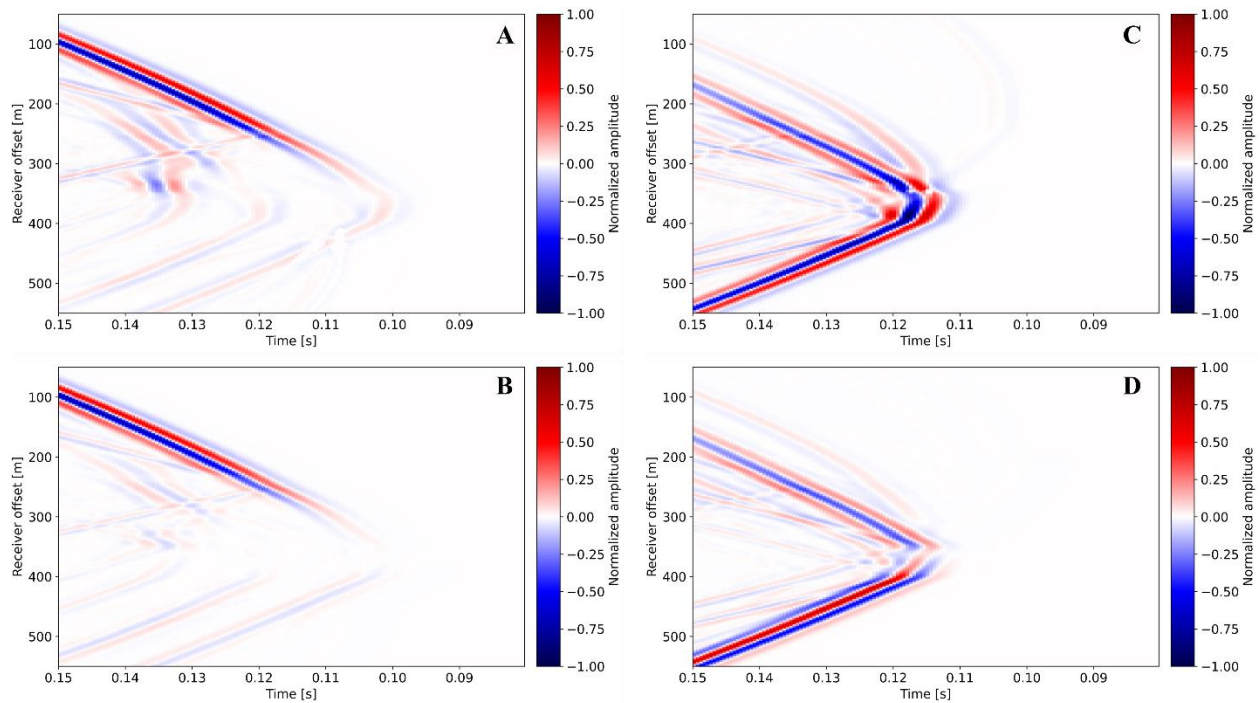


Figure 3. (A) baseline velocity model with the seismic cross-well survey geometry (B) monitor model with unstructured mesh. The black rectangle indicates the region of interest. Sources are depicted with yellow stars and receivers with green triangles. The CO₂ plume is indicated with a red arrow and the injection well with a black arrow.

191 We then compute the data difference and add uncorrelated Gaussian noise to
192 generate observations \mathbf{d}^{obs} . The noise has zero mean and a standard deviation equal
193 to 5% of the root-mean-square (RMS) amplitude of the noise-free data difference.
194 Figure 4 shows the observed (true) data difference between the baseline and monitor
195 data.

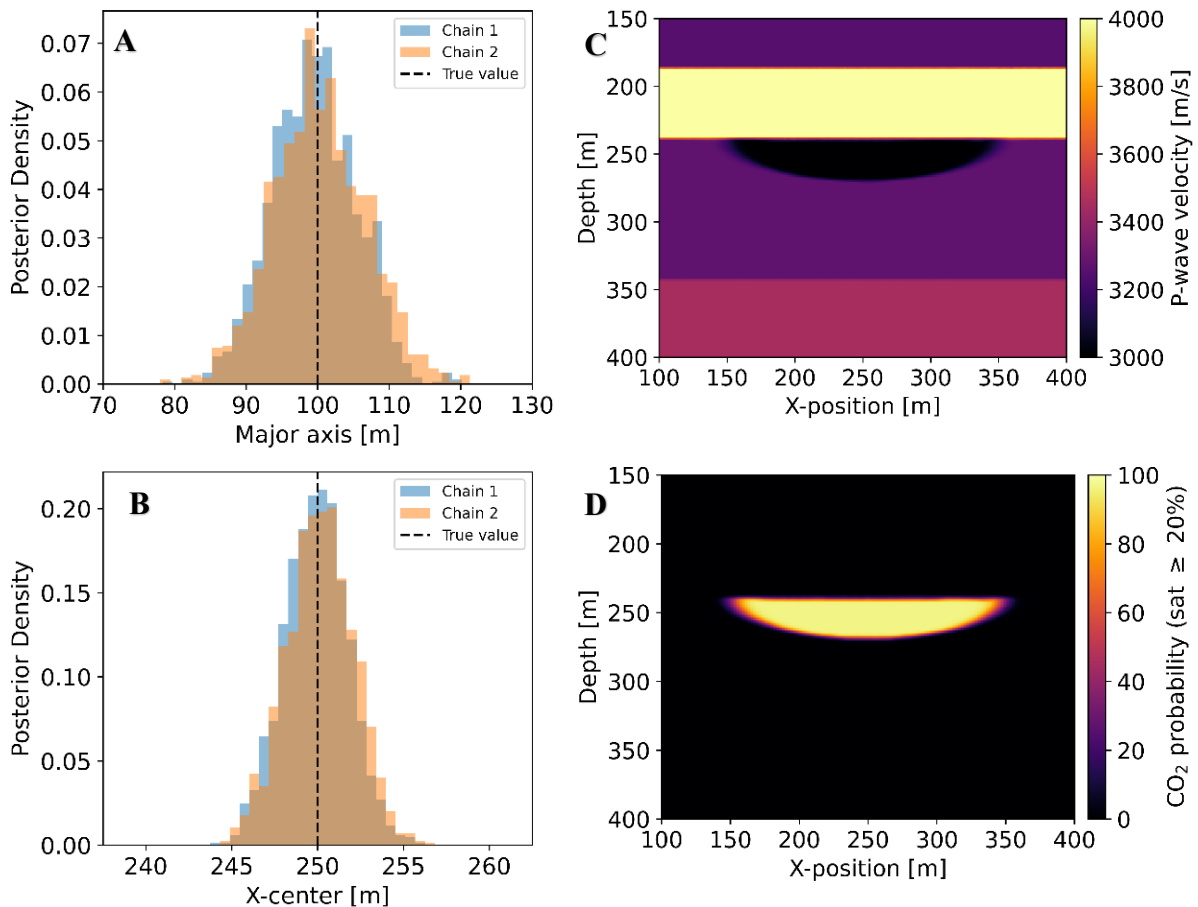


196

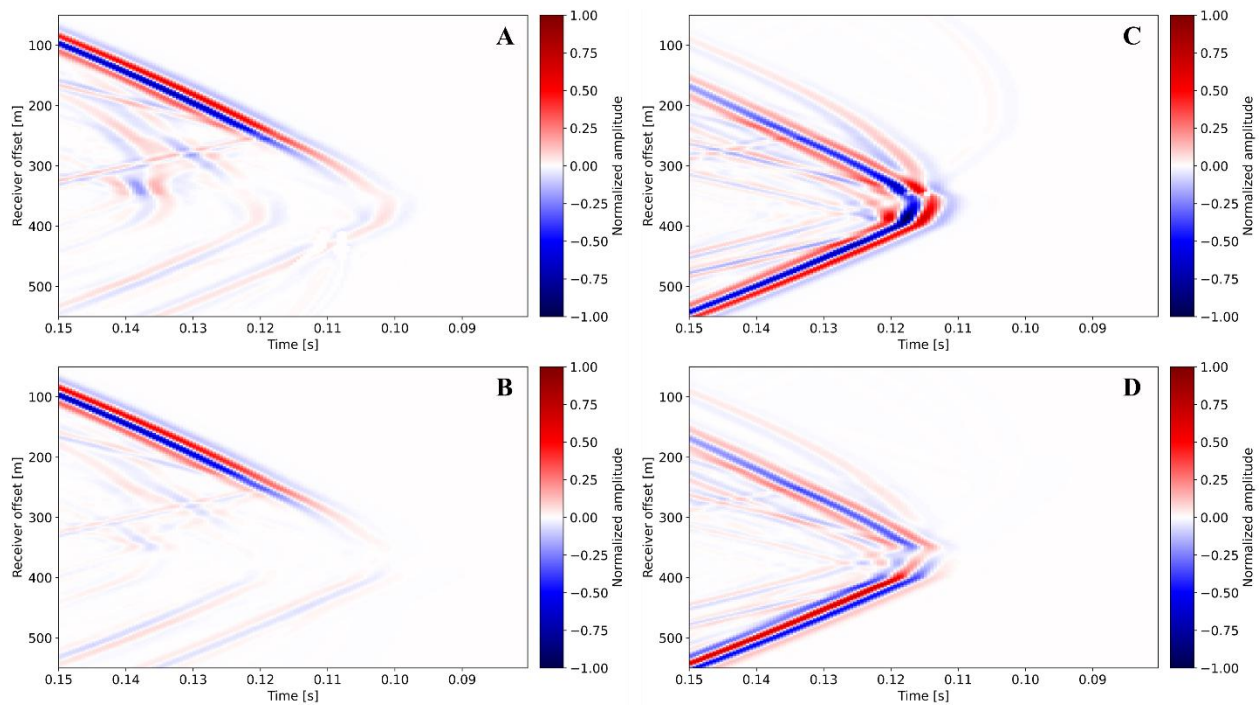
197 *Figure 4. Displacement data difference between baseline and monitor data. (A) shot 1, X-component, (B)*
 198 *shot 1, Z-component, (C) shot 2, X-component, and (D) shot 2, Z-component.*

199 To estimate the posterior distribution of the model parameters (i.e., ellipse center
 200 and major radius here), we run two independent Markov chains, each drawing 5,000
 201 samples. Figure 5a and 5b show the recovered posterior PDF for each parameter in
 202 both chains, respectively. We have acceptance rates of 21 and 23%. We discarded
 203 the first 5% of samples in each chain as the burn-in period, and we applied an
 204 adaptive sampling mechanism between 20% and 70% of the iterations. Figure 5
 205 shows our inversion results. From the histograms in Figure 5a and 5b we see that the
 206 chains have converged to the same distributions, the data constrain the model well,
 207 and that the mean recovered model agrees well with the true model. Figure 5c
 208 illustrates the average P-wave velocity model from the last 30% of the first chain.
 209 Figure 5d shows the interface-presence map, which is calculated based on a sigmoid

210 membership function to represent the spatial probability of CO₂ saturation above
211 20% from the last 30% of the first chain (Hong and Lee 1996). Figure 5 closely
212 matches the true model. Furthermore, Figure 6 illustrates the differences between
213 the true baseline data and the monitored data obtained from the recovered maximum
214 a posteriori (MAP) estimate of the first chain. A comparison between Figure 6 and
215 Figure 4 shows a close agreement between the two sets of results. Our findings
216 indicate that the plume is well recovered, establishing a robust foundation for our
217 next example.



218 *Figure 5. Histograms of (A) the major axis and (B) the X-position of the ellipse center, (C) the average P-*
219 *wave velocity model generated from the last 30% of accepted samples, and (D) the spatial probability of*
220 *CO₂ saturation levels higher than 20%, derived from the last 30% of samples in the first Markov chain.*



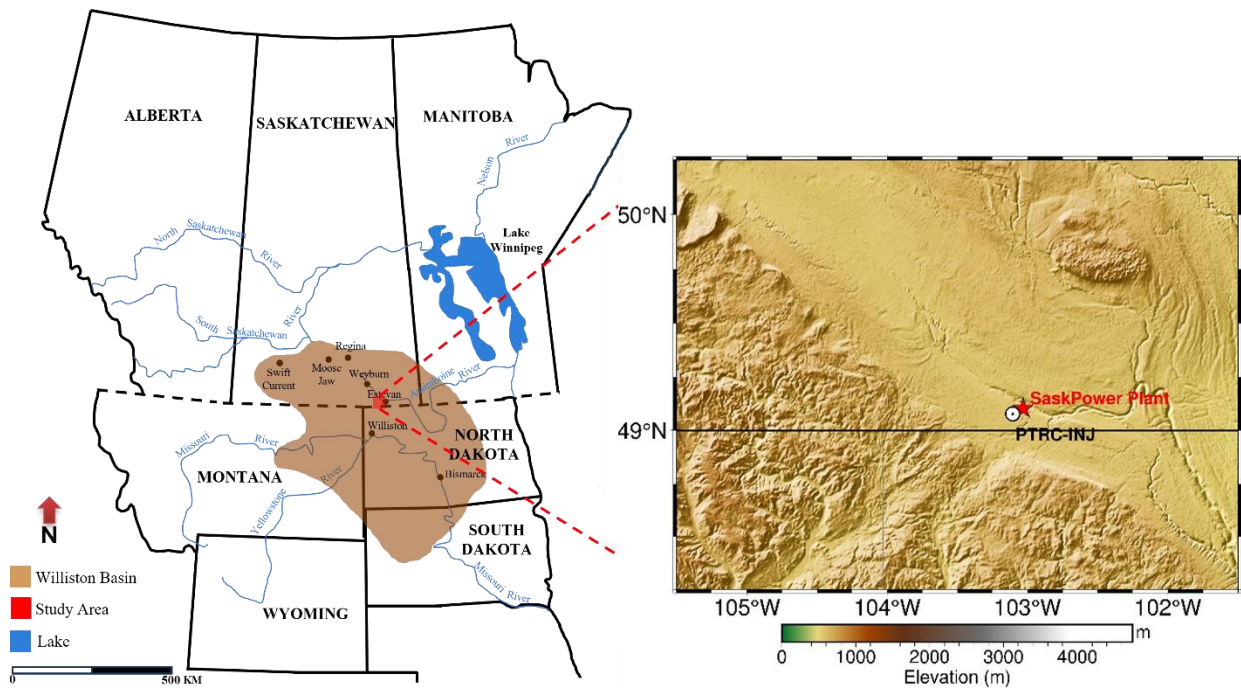
221
222 *Figure 6. Displacement data difference between the true baseline and recovered monitor data from the*
223 *MAP of the first Markov chain. (A) shot 1, X-component, (B) shot 1, Z-component, (C) shot 2, X-component,*
224 *and (D) shot 2, Z-component. The corresponding observed displacement difference data used in the*
225 *inversion are shown in Figure 4..*

226 For this example, using two NVIDIA RTX Quadro 6000 GPUs, each candidate
227 proposal evaluation takes about 18 seconds for two seismic sources using a Ricker
228 wavelet with a dominant frequency of 150 Hz.

229 **Field-scale FWI**

230 Our target area in this study is the Aquistore CO₂ storage project located in
231 Saskatchewan, Canada. The Aquistore site stores over 600,000 tonnes of CO₂ from
232 the SaskPower Boundary Dam coal-fired power plant. CO₂ injection started in April
233 2015 using one injection well and has been monitored since using various methods

234 (Roach and White 2018; Vahidinia et al. 2024). The Aquistore reservoir is a brine-
235 saturated saline clastic sequence positioned directly above the Precambrian
236 crystalline basement located in the Williston basin. Both the Deadwood Formation,
237 a silty to shaley sandstone, and the Black Island Sandstone were selected for CO₂
238 injection due to their favorable physicochemical properties (White et al. 2016).
239 Within this area, there are two sealing units: (1) the Winnipeg or Icebox (shale)
240 formation and (2) the Prairie evaporites. Figure 7 shows the location of the Williston
241 basin, Aquistore project, and the injector well named PTRC-INJ.



243 *Figure 7. Map showing the location of the Aquistore storage site within the Williston basin. The red star*
244 *illustrates the SaskPower plant and white circle shows the injector well PTRC-INJ.*

245 For our seismic and rock-physics simulations for the Aquistore project, we use the
246 same physical characteristics and properties as Table 1. We estimated these values

247 based on the available literature (White 2009; Roach and White 2018; Mavko et al.
248 2020; Vahidinia et al. 2024) for a deep saline reservoir with 6% porosity.

249 *Table 1. Mineral and fluid properties used in Gassmann substitution.*

Property	Value
Dominant mineral (matrix)	Quartz
Porosity (ϕ)	6 (%)
Pressure (P)	40 (MPa)
Temperature (T)	120 ($^{\circ}$ C)
Mineral bulk modulus (K_0)	32 (GPa)
Brine bulk modulus (K_w)	2.81 (GPa)
CO ₂ bulk modulus (K_g)	0.016 (GPa)
Mineral density (ρ_0)	2560 (kg/m ³)
Brine density (ρ_w)	1050 (kg/m ³)
CO ₂ density (ρ_g)	680 (kg/m ³)

250 In this example, we generate an asymmetric CO₂ plume, with two nodes constrained
251 to move freely along the Winnipeg horizon, while the remaining three are permitted
252 to vary within the spatial bounds of the reservoir (Deadwood Formation). Figure 8A
253 presents the baseline P-wave velocity model and the surface seismic acquisition
254 geometry, while Figure 8B shows the perturbation in the monitor model due to CO₂
255 injection.

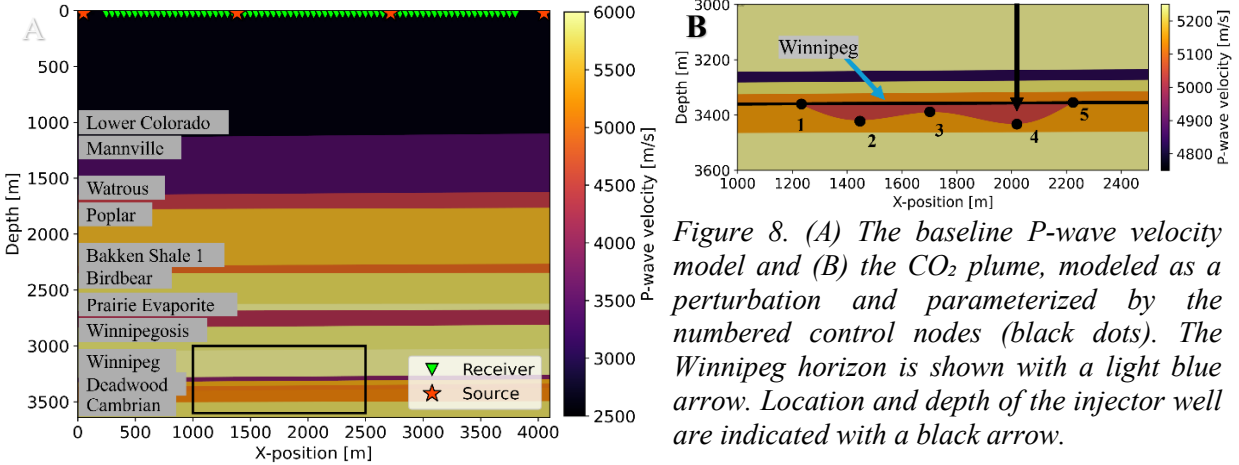
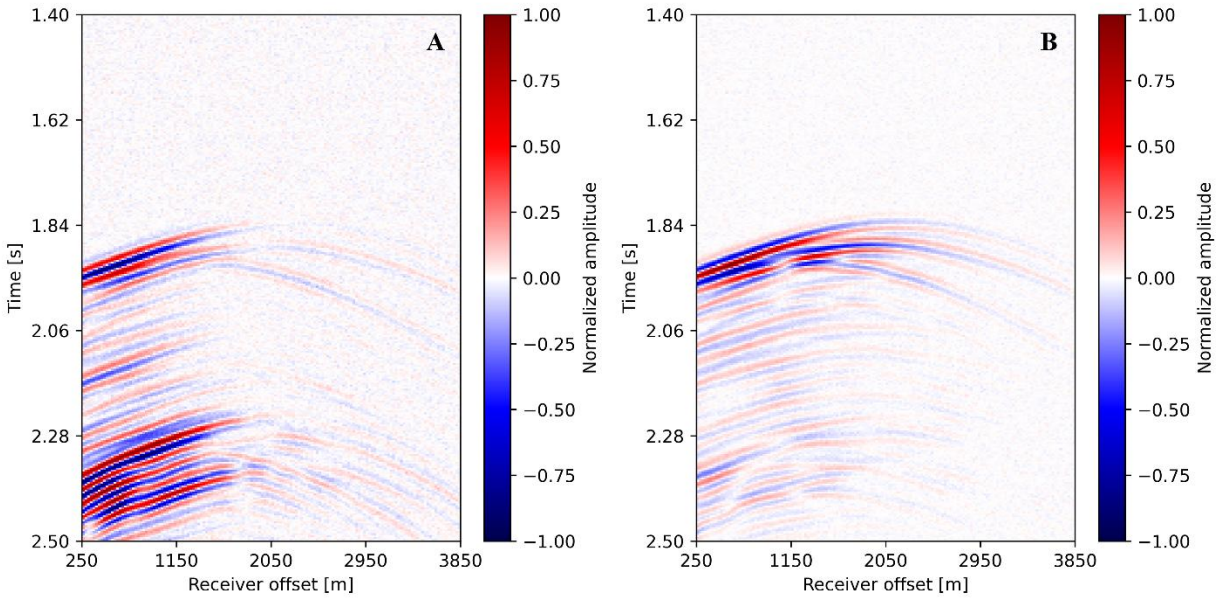


Figure 8. (A) The baseline P-wave velocity model and (B) the CO₂ plume, modeled as a perturbation and parameterized by the numbered control nodes (black dots). The Winnipeg horizon is shown with a light blue arrow. Location and depth of the injector well are indicated with a black arrow.

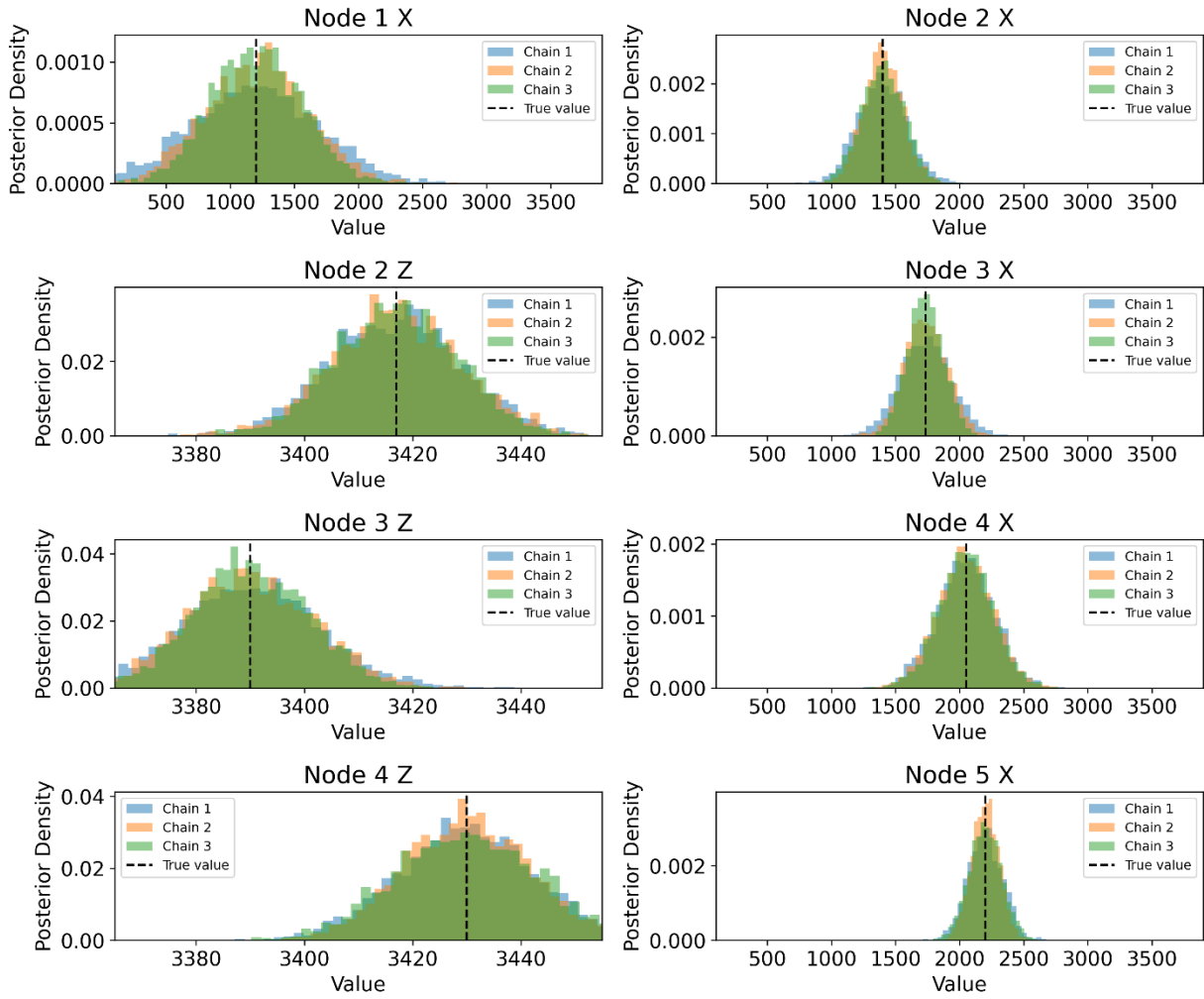
256 To generate the observations, we simulated an elastic seismic response for a duration
 257 of 2.5 seconds using a Ricker wavelet with a dominant frequency of 20 Hz across
 258 four equally spaced shots at the surface. Then, we subtracted the baseline data and
 259 following standard practices in Bayesian FWI studies (Hu et al. 2025), added 15%
 260 RMS-scaled uncorrelated Gaussian noise which resulted in an approximate signal-
 261 to-noise ratio of 16 dB. Figure 9 illustrates the observed data difference for one of
 262 the available seismic shots.



263

264 *Figure 9. Observed displacement data difference between prior and post injection stages for one of the*
 265 *shots. (A) X-component and (B) Z-component.*

266 To estimate the posterior PDF of our model parameters, we ran three independent
 267 Markov chains, with three different initializations. Each chain was run for 10,000
 268 samples, with the first 5% discarded as the burn-in period. Adaptive MH updates
 269 were applied between 20 and 70% of the iterations. The acceptance rates for the
 270 three chains were 21, 22, and 21%, respectively. Figure 10 shows the histograms of
 271 all three chains for each parameter defined in Figure 8b.

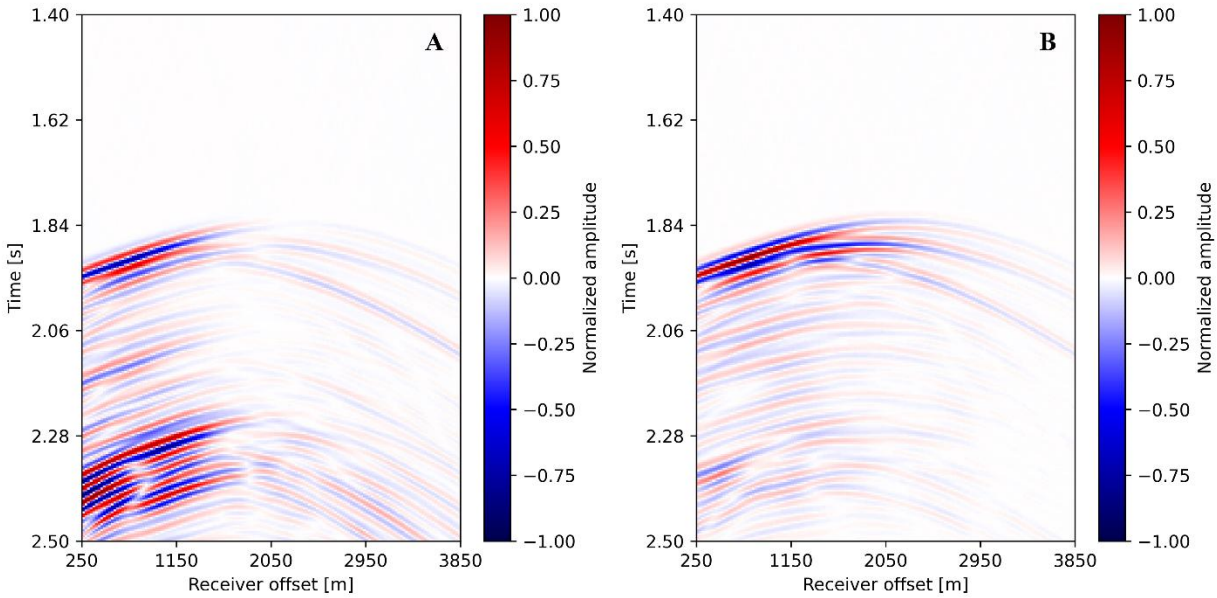


272

273 *Figure 10. Recovered posterior distributions for each parameter, presented as histograms, and labeled*
 274 *consistently with Figure 8b.*

275 Figure 11 shows the recovered displacement difference data calculated from the

276 MAP estimate of the second chain.

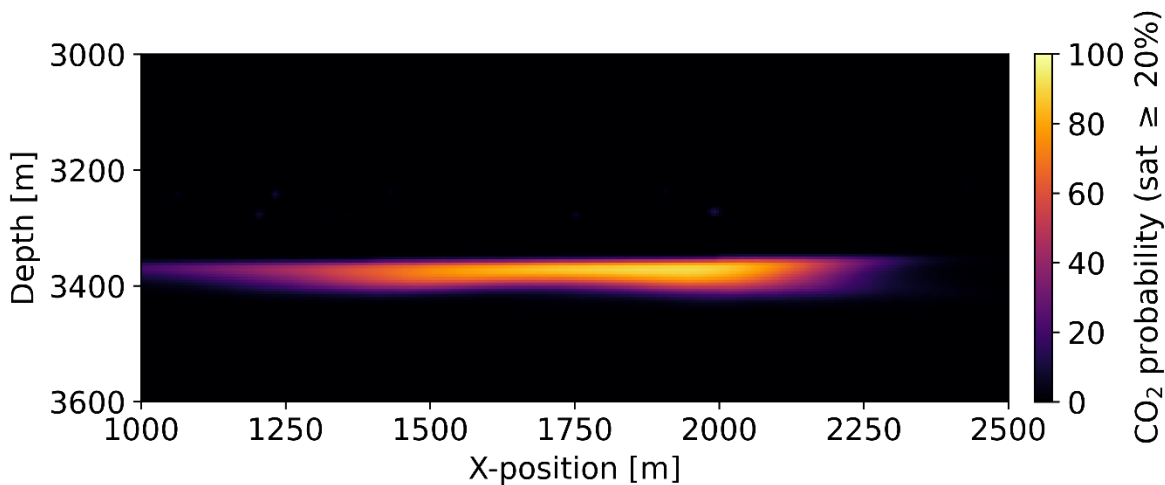


277

278 *Figure 11. Predicted time-lapse displacement difference data obtained by forward modeling the MAP*
 279 *estimate from the second Markov chain. (A) X-component and (B) Z-component. The corresponding*
 280 *observed displacement difference data used in the inversion are shown in Figure 9.*

281 Figure 12 illustrates the spatial probability of CO₂ saturation levels at or above 20%

282 derived from the last 30% of samples in the second chain.



283 *Figure 12. Spatial probability of CO₂ saturation levels higher than 20% based on the last 30% of samples*
 284 *from the second chain.*

285 In addition to visual inspection of the histograms illustrated in Figure 10, to evaluate

286 convergence between our chains, we calculated the Gelman-Rubin statistics. This

287 measures if multiple chains with different initializations converge to the same
288 distribution by comparing the variance within each chain to the variance between
289 chains. Its optimal value is between 1.0 and 1.1, with values closer to 1.0 indicating
290 better convergence (Gelman and Rubin 1992). With the average Gelman–Rubin
291 diagnostic value of 1.05 across chains for all parameters together with the visual
292 comparison between the spatial distribution of CO₂ shown in Figure 12 compared to
293 the ground truth shown in Figure 8b, we conclude that the data constrained each
294 individual node reasonably well, given the noise. Also the resulting posteriors,
295 illustrated in Figure 10, are consistent across chains indicating that the sampling
296 adequately explored the parameter space. A larger variance is observed for node 1
297 compared to node 5, where seismic sensitivity decreases due to the wedge effect,
298 which is consistent with our expectation from seismic data resolution (Kallweit and
299 Wood 1982; Sheriff and Geldart 1995; Zou et al. 2018).

300 For this specific example, using four NVIDIA RTX Quadro 6000 GPUs, each
301 forward simulation takes about 31 seconds. With 12 GPUs, 12 CPU cores and 8GB
302 of memory, a complete MCMC run with three independent parallel chains, each
303 containing 10,000 samples, ran in less than 80 hours of wall-clock time.

304 **Discussion**

305 Numerical feasibility is a key consideration in UQ studies using sampling methods,
306 where evaluating hundreds of thousands of candidate models is typically required.
307 In geophysical UQ studies where the forward solve is computationally expensive,
308 the number of DoF plays a critical role. A large number of DoF significantly
309 increases the number of iterations needed for sampling methods such as MCMC to
310 reach equilibrium (Roberts and Rosenthal 2001). Hence, keeping the number of DoF
311 small is key to reducing computational cost and sampling effort (Brooks et al. 2011;
312 Kotsi et al. 2020). Such strategies not only facilitate the use of sampling-based
313 methods for UQ but also can potentially enhance the practicality and efficiency of
314 other types of UQ methods such as variational inference approaches as they reduce
315 the dimensionality. Building on this concept, we proposed a rock-physics-guided
316 parameter reduction strategy for monitoring CO₂ plumes using seismic methods.
317 Although demonstrated here for seismic monitoring, in principle, the approach can
318 be extended to other geophysical inverse problems, as long as appropriate *a priori*
319 information is available.

320 While our framework can give credible UQ results at a practical computational cost,
321 there are a few methodological aspects to keep in mind. Although in our
322 experiments, we fixed the number of control-nodes, in principle we can have
323 flexibility in the number and configuration of control nodes, categorized into two

324 types: (1) anchor nodes and (2) inserted nodes. Anchor nodes are the initial nodes,
325 but the inserted nodes can be introduced dynamically during sampling, making our
326 method particularly suitable for trans-dimensional MCMC applications, where the
327 number of model parameters is itself an unknown (Sambridge et al. 2006; Bodin et
328 al. 2012; Sen and Biswas 2017). If the proposed representation is too restrictive,
329 complex plume geometries may not be fully captured, which can introduce model
330 bias and affect the resulting posterior estimates. In such cases, increasing the number
331 of control nodes provides additional flexibility, but at the cost of higher
332 dimensionality and potentially reduced sampling efficiency. This trade-off
333 highlights the importance of balancing model complexity and data sensitivity,
334 particularly in monitoring applications where plume evolution is expected to be
335 relatively smooth (Arts et al. 2004; Yordkayhun et al. 2009; Harvey et al. 2022).
336 Because we use cubic splines, the inserted nodes do not have to be evenly spaced,
337 which allows greater adaptability in modeling complicated geological features and
338 geometries. As additional nodes are introduced, the reconstructed geometry gains
339 flexibility, allowing complex plume shapes to be represented. Based on our
340 experiments where the number of control nodes was fixed, it appears effective to
341 start with a small number of nodes and gradually increase the number of nodes. This
342 strategy could be used in trans-dimensional methods, where the number of nodes
343 can change adaptively.

344 Another important extension is to treat the elastic properties within the plume as
345 unknown parameters to be inferred, rather than keeping them fixed. This can be done
346 depending on the *a priori* information available. Uncertainty in rock-physics
347 relationships and baseline elastic properties can also propagate into the inferred
348 plume geometry and posterior estimates. These effects could be incorporated within
349 a hierarchical Bayesian inversion framework for example, where rock-physics
350 parameters and baseline uncertainties are treated as additional unknowns. For
351 instance, in a cross-well scenario where only transmitted waves are relevant,
352 allowing the P-wave velocity to vary may lead to two outcomes: (1) the recovered
353 plume becomes wider but has a lower velocity, or (2) the plume appears smaller than
354 its actual size but with a higher velocity. In such cases, choosing the prior covariance
355 structures and the number of control-nodes to balance model flexibility with stability
356 and computational efficiency becomes critical.

357 Another key challenge is the heterogeneity of the plume. In this case, if the
358 heterogeneity is known (e.g., a linear lateral gradient), then it can be implemented
359 within our framework where the set of candidate models not only has the location of
360 the control-nodes but also contains information about the internal lateral velocity
361 gradient. If the heterogeneity within the plume is irregular or chaotic, then a
362 cooperative framework combining our approach with a cell-based (e.g., Voronoi)
363 strategy could be implemented.

364 By demonstrating the capability of our method to reconstruct the shape of a CO₂
365 plume, we recommend its application to both enhanced oil recovery (EOR) sweep
366 operations and CO₂ injection in deep saline aquifers. However, it is important to note
367 that it is the collective effect of the nodes and the connecting facets (i.e., the curves)
368 that influences the data; thus, as with most geophysical methods, the achievable
369 resolution ultimately depends on the data quality and coverage. Finally, the
370 numerical results illustrate that our framework effectively recovers the shape of an
371 anomalous body and quantifies the uncertainty of the reconstructed geometry. These
372 results highlight the potential of the proposed approach for reliable and
373 computationally feasible UQ in large-scale subsurface monitoring applications.

374 **Conclusion**

375 Using the rock physics of injected CO₂, we developed an efficient parameterization
376 scheme for UQ that significantly reduces the number of DoF and, consequently, the
377 number of samples required for convergence within the MCMC framework. By
378 representing the plume geometry with cubic splines controlled by a limited set of
379 nodes and fixing the elastic properties of the plume, our method accurately
380 reconstructs the CO₂ plume shape and quantifies associated uncertainties such as its
381 spatial extent. This parameter reduction enables the practical use of sampling-based
382 methods for large-scale CCS projects, overcoming the prohibitive computational
383 cost typically associated with conventional dense discretization schemes (i.e., space

384 filling cells). The demonstrated capability of our framework highlights its potential
385 for reliable and computationally feasible UQ in large-scale subsurface monitoring
386 applications. Although we demonstrated this efficiency within the McMC
387 framework, future work will extend this approach to variational inference methods
388 to further enhance scalability and enable near-real-time applicability.

389 **Acknowledgment**

390 We are grateful to Partha Routh and another anonymous reviewer for their
391 constructive feedback on an earlier version of this manuscript. This work was
392 supported by TotalEnergies E&P USA LLC and a grant from the Natural Sciences
393 and Engineering Research Council of Canada (NSERC), [funding reference number
394 20220503]. We gratefully acknowledge Paul Williamson, Bertrand Denel, and Yen
395 Sun from TotalEnergies E&P for valuable insights. We also thank Don White from
396 Natural Resources Canada (NRCan) for providing data and thoughtful discussions.
397 We also thank Xingda Jiang for helpful discussions. This research was enabled in
398 part by support provided by ACENET (ace-net.ca) and the Digital Research Alliance
399 of Canada (alliancecan.ca).

400 **Data and materials availability**

401 Data associated with this research are available and can be obtained by contacting
402 the corresponding author.

403 **References**

- 404 Arts, Rob, Ola Eiken, Andy Chadwick, Peter Zweigel, L Van der Meer, and B Zinszner. 2004.
405 “Monitoring of CO₂ Injected at Sleipner Using Time-Lapse Seismic Data.” *Energy* 29 (9–10):
406 1383–92.
- 407 Asnaashari, Amir, Romain Brossier, Stéphane Garambois, François Audebert, Pierre Thore, and
408 Jean Virieux. 2015. “Time-Lapse Seismic Imaging Using Regularized Full-Waveform Inversion
409 with a Prior Model: Which Strategy?” *Geophysical Prospecting* 63 (1): 78–98.
- 410 Asnaashari, Amir, Romain Brossier, Stéphane Garambois, Jean Virieux, François Audebert, and
411 Pierre Thore. 2012. “Time-Lapse Imaging Using Regularized FWI: A Robustness Study.” *SEG*
412 *International Exposition and Annual Meeting*, SEG-2012.
- 413 Bartels, Richard H, John C Beatty, and Brian A Barsky. 1995. *An Introduction to Splines for Use*
414 *in Computer Graphics and Geometric Modeling*. Morgan Kaufmann.
- 415 Bijani, Rodrigo, Peter G Lelièvre, Cosme F Ponte-Neto, and Colin G Farquharson. 2017.
416 “Physical-Property-, Lithology-and Surface-Geometry-Based Joint Inversion Using Pareto Multi-
417 Objective Global Optimization.” *Geophysical Journal International* 209 (2): 730–48.
- 418 Biot, Maurice A. 1941. “General Theory of Three-Dimensional Consolidation.” *Journal of Applied*
419 *Physics* 12 (2): 155–64.
- 420 Bodin, Thomas, Malcolm Sambridge, Nick Rawlinson, and Pierre Arroucau. 2012.
421 “Transdimensional Tomography with Unknown Data Noise.” *Geophysical Journal International*
422 189 (3): 1536–56.

423 Brooks, Steve, Andrew Gelman, Galin Jones, and Xiao-Li Meng. 2011. *Handbook of Markov*
424 *Chain Monte Carlo*. CRC press.

425 Coreform Cubit 2024.3. 2024. “Coreform Cubit (Version 2024.3) [Computer Software].” Orem,
426 UT. <http://coreform.com>.

427 Dorn, Oliver, and Yifan Wu. 2021. “Shape Reconstruction in Seismic Full Waveform Inversion
428 Using a Level Set Approach and Time Reversal.” *Journal of Computational Physics* 427: 110059.

429 Egorov, Anton, Roman Pevzner, Andrej Bóna, et al. 2017. “Time-Lapse Full Waveform Inversion
430 of Vertical Seismic Profile Data: Workflow and Application to the CO2CRC Otway Project.”
431 *Geophysical Research Letters* 44 (14): 7211–18.

432 Entezar-Saadat, V, A Khan Mohammadi, B Denel, C Farquharson, and A Malcolm. 2025. “Joint
433 Bayesian Seismic-Electromagnetic Inversion for CO2 Monitoring: A Synthetic Case Study from
434 the Johansen Formation.” *86th EAGE Annual Conference & Exhibition 2025* (1): 1–5.

435 Fichtner, Andreas, Brian LN Kennett, Heiner Igel, and Hans-Peter Bunge. 2009. “Full Seismic
436 Waveform Tomography for Upper-Mantle Structure in the Australasian Region Using Adjoint
437 Methods.” *Geophysical Journal International* 179 (3): 1703–25.

438 Fichtner, Andreas, and Saule Simutè. 2018. “Hamiltonian Monte Carlo Inversion of Seismic
439 Sources in Complex Media.” *Journal of Geophysical Research: Solid Earth* 123 (4): 2984–99.

440 Galley, Christopher G, Peter G Lelièvre, and Colin G Farquharson. 2020. “Geophysical Inversion
441 for 3D Contact Surface Geometry.” *Geophysics* 85 (6): K27–45.

442 Gassmann, Fritz. 1951. “Über Die Elastizität Poroser Medien.” *Vierteljahrsschrift Der*
443 *Naturforschenden Gesellschaft in Zurich* 96: 1–23.

444 Gelman, Andrew, Walter R Gilks, and Gareth O Roberts. 1997. “Weak Convergence and Optimal
445 Scaling of Random Walk Metropolis Algorithms.” *The Annals of Applied Probability* 7 (1): 110–
446 20.

447 Gelman, Andrew, and Donald B Rubin. 1992. “Inference from Iterative Simulation Using Multiple
448 Sequences.” *Statistical Science* 7 (4): 457–72.

449 Haario, Heikki, Eero Saksman, and Johanna Tamminen. 2001a. “An Adaptive Metropolis
450 Algorithm.” *Bernoulli* 7 (2): 223–42. <https://doi.org/10.2307/3318737>.

451 Haario, Heikki, Eero Saksman, and Johanna Tamminen. 2001b. *An Adaptive Metropolis*
452 *Algorithm*.

453 Harvey, Stephen, Jonathan Hopkins, Henning Kuehl, Simon O’Brien, and Albena Mateeva. 2022.
454 “Quest CCS Facility: Time-Lapse Seismic Campaigns.” *International Journal of Greenhouse Gas*
455 *Control* 117: 103665.

456 Hastings, W Keith. 1970. *Monte Carlo Sampling Methods Using Markov Chains and Their*
457 *Applications*.

458 Hong, Tzung-Pei, and Chai-Ying Lee. 1996. “Induction of Fuzzy Rules and Membership
459 Functions from Training Examples.” *Fuzzy Sets and Systems* 84 (1): 33–47.

460 Hu, Shuhua, Zeyu Zhao, and Mrinal K Sen. 2025. “Bayesian Full Waveform Inversion Using
461 Adaptive Markov Chain Monte Carlo Methods.” *Geophysics* 90 (5): 1–140.

462 Kadu, Ajinkya, Tristan van Leeuwen, and Wim A Mulder. 2016. “Salt Reconstruction in Full-
463 Waveform Inversion with a Parametric Level-Set Method.” *IEEE Transactions on Computational*
464 *Imaging* 3 (2): 305–15.

465 Kallweit, RS, and LC Wood. 1982. "The Limits of Resolution of Zero-Phase Wavelets."
466 *Geophysics* 47 (7): 1035–46.

467 Komatitsch, Dimitri, and Jeroen Tromp. 1999. "Introduction to the Spectral Element Method for
468 Three-Dimensional Seismic Wave Propagation." *Geophysical Journal International* 139 (3): 806–
469 22.

470 Kotsi, M, A Malcolm, and G Ely. 2020. "Uncertainty Quantification in Time-Lapse Seismic
471 Imaging: A Full-Waveform Approach." *Geophysical Journal International* 222 (2): 1245–63.

472 Kotsi, Maria, and Alison Malcolm. 2017. "A Statistical Comparison of Three 4d Full-Waveform
473 Inversion Schemes." In *SEG Technical Program Expanded Abstracts 2017*. Society of Exploration
474 Geophysicists.

475 Lewis, Winston, Bill Starr, and Denes Vigh. 2012. "A Level Set Approach to Salt Geometry
476 Inversion in Full-Waveform Inversion." *SEG International Exposition and Annual Meeting*, SEG-
477 2012.

478 Li, Jinji, and Kristopher A Innanen. 2024. "Hamiltonian Monte Carlo Based Time-Lapse Seismic
479 FWI and Uncertainty Quantification in CO2 Monitoring: A VSP Feasibility Study." *SEG
480 International Exposition and Annual Meeting*, SEG-2024.

481 Macquet, Marie, Donald C Lawton, Amin Saeedfar, and Kirk G Osadetz. 2019. "A Feasibility
482 Study for Detection Thresholds of CO2 at Shallow Depths at the CaMI Field Research Station,
483 Newell County, Alberta, Canada." *Petroleum Geoscience* 25 (4): 509–18.

484 Mavko, Gary, Tapan Mukerji, and Jack Dvorkin. 2020. *The Rock Physics Handbook*. Cambridge
485 university press.

486 Metropolis, Nicholas, Arianna W Rosenbluth, Marshall N Rosenbluth, Augusta H Teller, and
487 Edward Teller. 1953. "Equation of State Calculations by Fast Computing Machines." *The Journal*
488 *of Chemical Physics* 21 (6): 1087–92.

489 Mito, Saeko, and Ziqiu Xue. 2011. "Post-Injection Monitoring of Stored CO₂ at the Nagaoka Pilot
490 Site: 5 Years Time-Lapse Well Logging Results." *Energy Procedia* 4: 3284–89.

491 Mohammadi, A Khan, V Entezar-Saadat, B Denel, A Malcolm, and C Farquharson. 2025a.
492 "Enhancing Uncertainty Quantification Performance via Deep Learning-Assisted Markov Chain
493 Monte Carlo." *86th EAGE Annual Conference & Exhibition 2025* (1): 1–5.

494 Mohammadi, A Khan, V Entezar-Saadat, B Denel, A Malcolm, and C Farquharson. 2025b.
495 "Quantifying Uncertainties in Monitoring Megatonne-Scale CO₂ Injection: A Synthetic Seismic
496 Study in the Appalachian Basin."

497 Mosegaard, Klaus, and Malcolm Sambridge. 2002. "Monte Carlo Analysis of Inverse Problems."
498 *Inverse Problems* 18 (3): R29.

499 Mosegaard, Klaus, and Albert Tarantola. 1995. "Monte Carlo Sampling of Solutions to Inverse
500 Problems." *Journal of Geophysical Research: Solid Earth* 100 (B7): 12431–47.

501 Peter, Daniel, Dimitri Komatitsch, Yang Luo, et al. 2011. "Forward and Adjoint Simulations of
502 Seismic Wave Propagation on Fully Unstructured Hexahedral Meshes." *Geophysical Journal*
503 *International* 186 (2): 721–39.

504 Plessix, R-E, S Michelet, H Rynja, et al. 2010. "Some 3D Applications of Full Waveform
505 Inversion." *72nd EAGE Conference and Exhibition-Workshops and Fieldtrips*, cp-162.

506 Prasad, Manika, Stanislav Glubokovskikh, Thomas Daley, Similoluwa Oduwole, and William
507 Harbert. 2021. "CO2 Messes with Rock Physics." *The Leading Edge* 40 (6): 424–32.

508 Quei ber, Manuel, and Satish C Singh. 2013. "Full Waveform Inversion in the Time Lapse Mode
509 Applied to CO2 Storage at Sleipner." *Geophysical Prospecting* 61 (3): 537–55.

510 Ren , RM. 1986. "Gravity Inversion Using Open, Reject, and 'Shape-of-Anomaly' Fill Criteria."
511 *Geophysics* 51 (4): 988–94.

512 Roach, Lisa AN, and DJ White. 2018. "Evolution of a Deep CO2 Plume from Time-Lapse Seismic
513 Imaging at the Aquistore Storage Site, Saskatchewan, Canada." *International Journal of*
514 *Greenhouse Gas Control* 74: 79–86.

515 Roberts, Gareth O, and Jeffrey S Rosenthal. 2001. "Optimal Scaling for Various Metropolis-
516 Hastings Algorithms." *Statistical Science* 16 (4): 351–67.

517 Sambridge, Malcolm, K Gallagher, Andrew Jackson, and Peter Rickwood. 2006. "Trans-
518 Dimensional Inverse Problems, Model Comparison and the Evidence." *Geophysical Journal*
519 *International* 167 (2): 528–42.

520 Sambridge, Malcolm, and Klaus Mosegaard. 2002. "Monte Carlo Methods in Geophysical Inverse
521 Problems." *Reviews of Geophysics* 40 (3): 3–1.

522 Schumaker, Larry L. 2015. *Spline Functions: Computational Methods*. SIAM.

523 Sen, Mrinal K, and Reetam Biswas. 2017. "Transdimensional Seismic Inversion Using the
524 Reversible Jump Hamiltonian Monte Carlo Algorithm." *Geophysics* 82 (3): R119–34.

525 Sen, Mrinal K, and Paul L Stoffa. 2013. *Global Optimization Methods in Geophysical Inversion*.
526 Cambridge University Press.

527 Sheriff, Robert E, and Lloyd P Geldart. 1995. *Exploration Seismology*. Cambridge university
528 press.

529 Tarantola, Albert. 2005. *Inverse Problem Theory and Methods for Model Parameter Estimation*.
530 SIAM.

531 Tromp, Jeroen, Dimitri Komatitsch, Qinya Liu, and others. 2008. “Spectral-Element and Adjoint
532 Methods in Seismology.” *Communications in Computational Physics* 3 (1): 1–32.

533 Uieda, Leonardo, and Valéria CF Barbosa. 2012. “Robust 3D Gravity Gradient Inversion by
534 Planting Anomalous Densities.” *Geophysics* 77 (4): G55–66.

535 Vahidinia, Shima, Alireza Rangriz Shokri, and Rick Chalaturnyk. 2024. “Assessment of Storage
536 Efficiency Factor of Deep Saline Aquifers Using Early 500 Ktonnes of Injected CO₂ at the
537 Aquistore CCS Site.” *SPE Annual Technical Conference and Exhibition?*, D031S045R004.

538 Vatankhah, Saeed, Peter G Lelièvre, and Jérémie Giraud. 2025. “Review of Advancements in
539 Geometry-Based Inversion of Geophysical Data Sets.” *Surveys in Geophysics*, 1–46.

540 Virieux, Jean, and Stéphane Operto. 2009. “An Overview of Full-Waveform Inversion in
541 Exploration Geophysics.” *Geophysics* 74 (6): WCC1–26.

542 White, DJ, CD Hawkes, and BJ Rostron. 2016. “Geological Characterization of the Aquistore CO₂
543 Storage Site from 3D Seismic Data.” *International Journal of Greenhouse Gas Control* 54: 330–
544 44.

545 White, Don. 2009. “Monitoring CO₂ Storage during EOR at the Weyburn-Midale Field.” *The
546 Leading Edge* 28 (7): 838–42.

547 Yordkayhun, Sawasdee, Ari Tryggvason, Ben Norden, Christopher Juhlin, and Björn Bergman.
548 2009. “3D Seismic Traveltime Tomography Imaging of the Shallow Subsurface at the CO₂ SINK
549 Project Site, Ketzin, Germany.” *Geophysics* 74 (1): G1–15.

550 Zhang, Fengjiao, Christopher Juhlin, Monika Ivandic, and Stefan Lüth. 2013. “Application of
551 Seismic Full Waveform Inversion to Monitor CO₂ Injection: Modelling and a Real Data Example
552 from the Ketzin Site, Germany.” *Geophysical Prospecting* 61: 284–99.

553 Zheglova, Polina, and Colin Farquharson. 2016. “Joint Level Set Inversion of Gravity and Travel
554 Time Data: Application to Mineral Exploration.” *SEG International Exposition and Annual
555 Meeting*, SEG-2016.

556 Zheglova, Polina, Peter G Lelièvre, and Colin G Farquharson. 2018. “Multiple Level-Set Joint
557 Inversion of Traveltime and Gravity Data with Application to Ore Delineation: A Synthetic
558 Study.” *Geophysics* 83 (1): R13–30.

559 Zou, Guangui, Zhiliang Xu, Suping Peng, and Feng Fan. 2018. “Analysis of Coal Seam Thickness
560 and Seismic Wave Amplitude: A Wedge Model.” *Journal of Applied Geophysics* 148: 245–55.

561